

Article

Numerical Study on Tandem-Rotor Autorotation in Forward Flight

Jiayu Wen, Yanguo Song ^{*}, Huanjin Wang  and Dong Han

College of Aerospace Engineering, Nanjing University of Aeronautics and Astronautics, Nanjing 210001, China

^{*} Correspondence: songyg@nuaa.edu.cn

Abstract: This work presents a systematic approach to analyzing the aerodynamic characteristics of tandem rotor forward autorotation considering rotor-to-rotor interference. The single-rotor computational model trimmed from a generic helicopter flight dynamics analysis program was used as the baseline model. The effectiveness of the baseline model is demonstrated by a comparison with data from wind tunnel tests performed in this work. The rotor disk angle of attack and driven moment distribution obtained by the modified model indicate the fact that the rotor acceleration is primarily caused by the higher angle of attack region of the disk. This is of great significance in the rotor blade design, in terms of the drag-to-lift ratio characteristics of the airfoil under different angle-of-attack ranges. The influence of wind speed, rotor shaft angle, and collective pitch on the steady-state rotor speed was then studied. The results show a nonlinear nature of the variation of steady rotor speed with collective pitch, which can cause a thrust control reverse problem during flight operations. To reveal the flow field details of rotor-to-rotor interference, the flow field Navier–Stokes equations of tandem rotor autorotation were solved. Computational results of both rotors' inflow velocities were considered when deriving the empirical model of interference. The refined interference model was compared to the wind tunnel test data of the tandem rotor autorotation and showed good performance. This synthetical methodology, which combines mechanism analysis with CFD-aided refinement and experiment verification, achieves a balance between computational costs and accuracy and thus can be readily applied to engineering practices.

Keywords: tandem helicopter; autorotation; rotor-to-rotor interference; wind tunnel experiment; computational fluid dynamics; flight dynamics



Citation: Wen, J.; Song, Y.; Wang, H.; Han, D. Numerical Study on Tandem-Rotor Autorotation in Forward Flight. *Aerospace* **2023**, *10*, 15. <https://doi.org/10.3390/aerospace10010015>

Academic Editor: Paul Bruce

Received: 24 November 2022

Revised: 15 December 2022

Accepted: 19 December 2022

Published: 24 December 2022



Copyright: © 2022 by the authors. Licensee MDPI, Basel, Switzerland. This article is an open access article distributed under the terms and conditions of the Creative Commons Attribution (CC BY) license (<https://creativecommons.org/licenses/by/4.0/>).

1. Introduction

The transportation network of modern cities is experiencing rapid development. People's demand for convenient and efficient urban and intercity transportation is increasing rapidly. At the same time, with the continuous development of electronic commerce, the demand for urban and intercity cargo transportation is also expanding. In addition, as the demand for new energy vehicles is gradually expanding, technology is also advancing rapidly. These three factors have created a need for efficient, long-endurance, heavy-lift Advanced Air Mobility (AAM) vehicles. The AAM industry with electric Vertical Takeoff and Landing (e-VTOL) aircraft as its dominant configuration has incomparable advantages over traditional aviation. For example, e-VTOL vehicles have fewer requirements for terminal infrastructure and area than traditional aircraft. As a result, the AAM industry with e-VTOL as its mainstay is attracting a large amount of capital investment. One of the key issues in the research on advanced e-VTOL aircraft is to improve its performance. Specifically, it is necessary to improve its hover efficiency, cruise efficiency, and cruise speed in order to obtain the best economic efficiency by improving the overall performance of the aircraft under limited battery energy density. Therefore, it is urgent to design a new configuration of rotorcraft, which can break the technical barriers of cruise speed and a load of traditional rotorcraft.

The cruise speed limitation suffered by conventional single-rotor configuration has forced researchers to shift their focus to new configurations such as tilt-rotors [1], coaxial, including Advancing Blade Concept (ABC) rotors [2–4], and compound helicopters [5–7]. Most of the current compound configurations have adopted a powered single-rotor scheme. The conventional helicopter speed limitation is released by slowing down the main rotor speed and making the fixed wing provide the majority of lift during high-speed conditions [8]. In order to increase both the speed and load ability, the novel configuration of tandem rotor compound autogyro inherits the high cruise speed of a compound helicopter, the heavy load capacity of a tandem rotor helicopter, and the high flight safety of an autogyro. In the research field of autogyros and gyroplanes, work on aerodynamics [9] and flight dynamics modeling [10] was performed by analyzing both autogyros and powerless descending helicopters [11]. In terms of the single-rotor case, a generic helicopter rotor model could be used to simulate the autorotation flight conditions, but additional experiments and analyses must be performed to deal with specific aircraft types. This work is thus driven and supported by the requirement for the designing of an e-VTOL tandem compound autogyro.

Existing methodologies for the aerodynamic interaction of rotorcrafts fall into the categories of experimental, theoretical, and computational fluid dynamics (CFD) approaches. In the experimental and empirical aspects, wind tunnel tests must be involved to investigate flight conditions other than hover. Particle image velocimetry (PIV), as a smoke flow visualization technique, can be performed to record the flow structure of the rotor wake and blade tip vortices. Le Pape et al. [12] studied the interference between the rotor and fuselage by means of PIV measurements during wind tunnel tests. Experiments on rotor-to-rotor interference of the multirotor system were conducted by Ramasamy [13]. Coaxial, tandem, and tilt-rotor configurations were taken into account. Without a wind tunnel, only hover performance loss factors were obtained. Brazinskas et al. [14] empirically studied the rotor-to-rotor interference of the overlapping propulsion system of a small-scaled unmanned aerial vehicle (UAV), with a focus on the partially overlapping rotors in low-Reynolds-number conditions. Wind tunnel tests were conducted by Li et al. [15] on a new configuration of unparallel-rotor multi-rotor UAV. The interaction between rotors was studied with varying parameters of the rotor plane relative angle and rotor spacing. The influence of the advance ratio, shaft angle, and lift offset on a rigid coaxial rotor was tested in the wind tunnel by Wang et al. [16]. From the theoretical perspective, blade element theory (BET) is prevalently adopted for its intrinsically simple nature, in-flight dynamics analysis, and flight simulation. In such applications, the rotor-induced velocity field must be modeled by certain means of inflow theories. Lee et al. [17] presented a new blade element momentum theory to iteratively solve the inflow fields of both rotors of the coaxial rotor system in hover. For the tandem rotor case, Guner et al. [18] studied the interference of CH-47D helicopter rotors to explain the discrepancy between the flight simulator and flight test results. The study showed that the inflow coupling of the twin rotors can be simulated by appropriately selecting the gains of the first harmonic inflow terms. In the computational field of research, Misiorowski et al. [19] solved the Navier–Stokes (N-S) equations with the detached-eddy simulation model to reveal the rotor-to-rotor interference of the quadcopter during edgewise flight. The lift reduction of each rotor was obtained for both cross and plus rotor configurations. The influence of rotor separation on the aerodynamic interaction of twin rotor configurations was studied with CFD by Healy et al. [20]. In addition to rotor-to-rotor interactions, rotorcraft-to-rotorcraft interactions were investigated by Tan et al. [21]. The flow field and airloads of a V-22 tiltrotor influenced by a CH-46 tandem rotor on the upwind were revealed by a vortex-based approach.

As a matter of fact, little attention has been paid to the tandem rotor interference under an autorotating condition by either of the above-mentioned methods. For this reason, as a requirement of preliminary design, it is desired to establish a comprehensive analysis methodology to investigate the rotor aerodynamics behavior, especially that of the rotor-to-rotor interference during autorotation. In order to be applied to the forthcoming parametric

design, performance estimation, flight dynamics, and control synthesis, the method derived for interference analysis should be less time- and resource-consuming. A synthetic approach combining mechanism analysis, CFD-aided refinement, and experimental verification is adopted to establish a systematical methodology. A baseline rotor model using blade element analysis and the Pitt–Peters dynamic inflow model of the single rotor was modified by adding an outer iterative solving loop of the rotor speed and Reynolds number to account for the changing Reynolds number effect caused by the drastic change in rotor speed during the transient process. The baseline model was then used to analyze the single-rotor forward autorotation behavior. Considering the wind speed, the rotor shaft angle, and collective pitch as variables, the variation of rotor speed with these parameters is provided. The influence of blade sectional lift-and-drag characteristics under different rotor speeds are studied through the angle of attack (AoA) distribution and the driven/driving region of the rotor disk. As the rear rotor is operated in the strong wake of the front rotor in tandem autorotation situations, an abrupt rotor speed drop can be seen in the rear rotor. The reduction of rotor speed thus causes a decrease in thrust, as the collective pitch increases. Because the total number of flight conditions and measurable states are limited in a wind tunnel experiment, and to further investigate the details of the interfered flow field, the computational fluid dynamics method was adopted to numerically solve the transient Navier–Stokes equation of this problem. A transient N-S solver of a second-order upwind scheme provided by FLUENT was used, with a pressure-velocity coupling scheme of the semi-implicit method for pressure-linked equations (SIMPLE) and a Menter shear stress transport (SST) k - ω turbulence model. The sliding mesh technique was utilized to simulate the rotor flow field, considering the stability and cost of time and computer resources. The detailed flow field reveals the mechanism of the interference on the rear rotor. Numerical results from CFD analysis were utilized by the coupled inflow model to perform model refinement of the single rotor, hence establishing an efficient approach for predicting the aerodynamic characteristics of this configuration.

2. Isolated Rotor HeliFDM Computational Model

2.1. Rotor Aerodynamics Model

This work utilized the rotor aerodynamics model from a generic helicopter flight dynamics analysis and simulation software HeliFDM. The individual center-spring-equivalent blade-flapping equation of motion can be written as follows [22]:

$$\ddot{\beta} + \left(\Omega^2 + \frac{K_\beta}{I_\beta} \right) \beta = \Omega^2 \frac{\rho c a_0 R^4}{2 I_\beta} \int_0^1 \left(U_T^2 \theta + U_T U_P \right) r_b dr_b \quad (1)$$

in which β is the rotor blade-flapping angle, Ω is the rotor rotational angular velocity, K_β is the center-spring rotor stiffness, I_β is the flapping moment of inertia, and $\rho c a_0 R^4 / I_\beta$ is the rotor Lock number. The gyroscopic acceleration term caused by the fuselage angular velocity was effectively ignored. U_P and U_T are non-dimensional blade elements' in-plane and normal velocities. These velocity components were integrated over the rotor disk and then iterated with the rotor inflow equations. The above rotor blade equation of motion was then described in the multi-blade coordinate, presented by Padfield [23], to be incorporated into the rotor aerodynamics model. The individual blade motion was transformed into multi-blade coordinates. Since only one-per-rev harmonic components exist in the case of a three-bladed rotor, three mode shapes in terms of disk coning β_0 , longitudinal cyclic flapping β_{1c} , and lateral cyclic flapping β_{1s} can be defined as follows:

$$\begin{aligned} \beta_0 &= \frac{1}{3} \sum_{i=1}^3 \beta_i, \\ \beta_{1c} &= \frac{2}{3} \sum_{i=1}^3 \beta_i \cos \psi_i, \\ \beta_{1s} &= \frac{2}{3} \sum_{i=1}^3 \beta_i \sin \psi_i \end{aligned} \quad (2)$$

With the above definition, individual blade-flapping equations of motion can be represented in multi-blade coordinates as:

$$\begin{bmatrix} \ddot{\beta}_0 \\ \ddot{\beta}_{1c} \\ \ddot{\beta}_{1s} \end{bmatrix} = -\Omega C_{M0} \begin{bmatrix} \dot{\beta}_0 \\ \dot{\beta}_{1c} \\ \dot{\beta}_{1s} \end{bmatrix} - \Omega^2 D_{M0} \begin{bmatrix} \beta_0 \\ \beta_{1c} \\ \beta_{1s} \end{bmatrix} + \Omega^2 H_{M0} \tag{3}$$

in which the coefficient matrices C_{M0} , D_{M0} , and H_{M0} were modified with the assumption of an untwisted blade and neglecting terms caused by fuselage angular motion, as follows:

$$C_{M0} = \begin{bmatrix} \frac{\gamma}{8} & 0 & \frac{1}{12}\gamma\mu \\ 0 & \frac{\gamma}{8} & 2 \\ \frac{1}{6}\gamma\mu & -2 & \frac{\gamma}{8} \end{bmatrix} \tag{4}$$

$$D_{M0} = \begin{bmatrix} \lambda_\beta^2 & 0 & 0 \\ \frac{1}{6}\gamma\mu & \lambda_\beta^2 - 1 & \frac{\gamma}{8} + \frac{\gamma\mu^2}{16} \\ 0 & -\frac{\gamma}{8} + \frac{\gamma\mu^2}{16} & \lambda_\beta^2 - 1 \end{bmatrix} \tag{5}$$

$$H_{M0} = \begin{bmatrix} \frac{1}{8}\gamma\theta_0(1 + \mu^2) + \frac{1}{6}\gamma\mu\theta_{1sw} + \frac{1}{6}\gamma(\mu_z - \lambda_0) - \frac{1}{12}\gamma\mu\lambda_{1sw} \\ \frac{1}{8}\gamma\theta_{1cw} \left(1 + \frac{\mu^2}{2}\right) - \frac{1}{8}\gamma\lambda_{1cw} \\ \frac{1}{3}\gamma\mu\theta_0 + \frac{1}{8}\gamma\theta_{1sw} \left(1 + \frac{3}{2}\mu^2\right) + \frac{1}{4}\gamma\mu(\mu_z - \lambda_0) - \frac{1}{8}\gamma\lambda_{1sw} \end{bmatrix} \tag{6}$$

In the above definitions, γ is the rotor Lock number, is the rotor advance ratio, μ_z is the total normalized rotor inflow, λ_β is the flap frequency ratio, $[\lambda_0 \ \lambda_{1cw} \ \lambda_{1sw}]$ are the uniform and first harmonic inflow components in wind axes, and $[\theta_0 \ \theta_{1cw} \ \theta_{1sw}]$ are the uniform and first harmonic rotor pitch controls.

The rotor model incorporated the blade element analysis and Pitt–Peters dynamic inflow model. A three-state Pitt–Peters dynamic inflow model [24] was adopted to solve the rotor-induced velocity field, the governing equation of which is given as follows:

$$\lambda = \lambda_0 + \bar{r}\lambda_{1s} \sin \psi + \bar{r}\lambda_{1c} \cos \psi$$

$$M \begin{bmatrix} \dot{\lambda}_0 \\ \dot{\lambda}_{1s} \\ \dot{\lambda}_{1c} \end{bmatrix} + L_{nl}^{-1} \begin{bmatrix} \lambda_0 \\ \lambda_{1s} \\ \lambda_{1c} \end{bmatrix} = \begin{bmatrix} C_T \\ C_{La} \\ C_{Ma} \end{bmatrix} \tag{7}$$

in which $[\lambda_0 \ \lambda_{1c} \ \lambda_{1s}]$ are the uniform and first harmonic inflow components in hub axes and C_T is the thrust coefficient. C_{La} and C_{Ma} are the coefficients of thrust and aerodynamic rolling and pitching moment, which induces the first harmonic terms of non-uniform inflow. M , the apparent mass matrix for untwisted blades, is

$$M = \begin{bmatrix} 8/3\pi & 0 & 0 \\ 0 & 16/45\pi & 0 \\ 0 & 0 & 16/45\pi \end{bmatrix} \tag{8}$$

and the nonlinear gains matrix is given by:

$$L_{nl} = \begin{bmatrix} 1/2 & 0 & -\frac{15\pi}{64} \sqrt{\frac{1-\sin\alpha}{1+\sin\alpha}} \\ 0 & \frac{4}{1+\sin\alpha} & 0 \\ \frac{15\pi}{64} \sqrt{\frac{1-\sin\alpha}{1+\sin\alpha}} & 0 & \frac{4\sin\alpha}{1+\sin\alpha} \end{bmatrix} \cdot \begin{bmatrix} V_T & 0 & 0 \\ 0 & V & 0 \\ 0 & 0 & V \end{bmatrix}^{-1}$$

$$V = \frac{\mu^2 + (2\lambda_0 - \mu_z)(\lambda_0 - \mu_z)}{V_T}$$

$$\tag{9}$$

in which α is the wake angle and V_T is the total resultant velocity through the rotor disk.

The simulation process can be summarized in Figure 1. Initial guesses of the rotor states, including the rotor speed, disk inflow ratio and flapping angles, and angular velocities were fed to the rotor model along with three independent test variables, the wind speed V_x , the rotor shaft angle θ , and the blade pitch control θ_0 . Blade element aerodynamic loads on a grid of 36 blade span stations by 72 disk azimuth stations were integrated to provide the aerodynamics coefficients. The airfoil section lift and drag coefficients were treated as variables of the angle of attack and Reynolds number. The varying Reynolds number effect will be discussed in the next section. Derivatives of the rotor inflow states and blade-flapping states were then calculated with the theory presented above. A $C_t - \lambda - \beta$ iterative scheme was utilized to find the solutions to the system. The derivative of rotor speed was then computed by the rotor angular equation of motion. Rotor speed was then iteratively solved with the Reynolds number through a similar scheme of the $C_t - \lambda - \beta$ iteration scheme. Numerical integration of derivatives of the rotor states and angular velocity by the ODE4 Runge–Kutta formulae was performed to obtain the states of the next computational frame. The criterion for finding the steady-state rotor speed is when its derivative is less than $1 \times 10^{-3} \text{ rev/s}^2$.

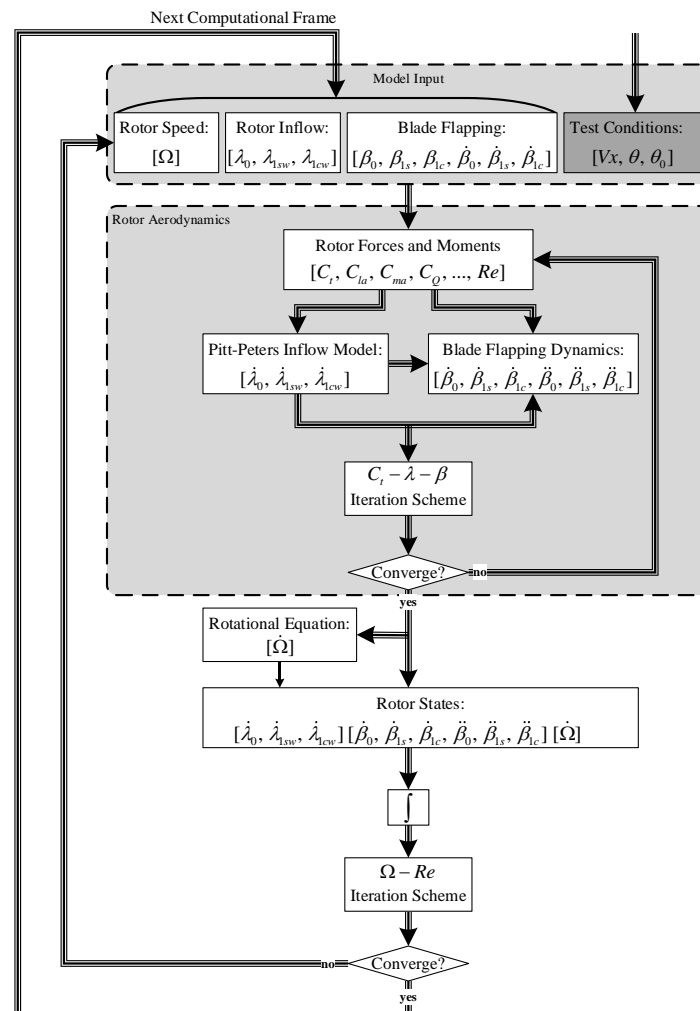


Figure 1. Rotor aerodynamics computational model.

2.2. Varying Reynolds Number Effect

The Reynolds number has a significant impact on the blade element loads. For conventional shaft-driven helicopter rotor aerodynamics modeling, however, less attention was paid to the effect of varying Reynolds numbers on the rotor aerodynamic force and moment, since, for powered rotors, the change in rotational speed of the rotor is usually

small, which makes the impact of changing Reynolds number less significant. However, for problems involving autorotation, especially the experiment taken in this work, the rotor speed can vary from nearly 100 rpm to 1000 rpm (Reynolds number in the range of $1 \times 10^4 \leq Re \leq 6 \times 10^5$), which can cause a drastic change in Reynolds number, as shown in Figure 2. The blade airfoil aerodynamic characteristics, especially the drag coefficient, are significantly impacted by the Reynolds number [25]; hence, the transient behavior as well as the steady-state rotational speed analysis cannot be analyzed without considering the variation in the Reynolds number.

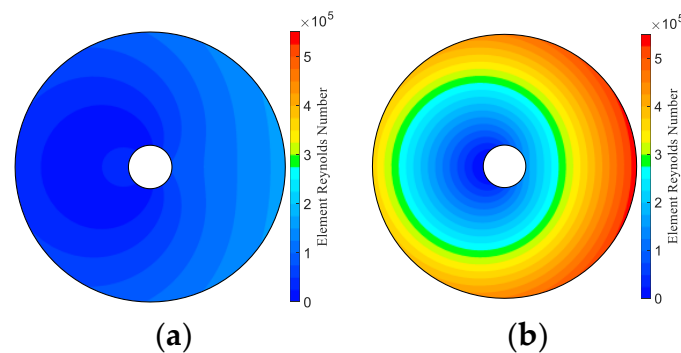


Figure 2. Reynolds number distribution at different rotor speeds: (a) $\Omega = 170$ rpm; (b) $\Omega = 800$ rpm.

Since an interaction exists between the Reynolds number and the rotor speed, the varying effect of the Reynolds number cannot be treated with a simple open-loop computational strategy. Instead, an outer loop of the Reynolds number and rotor speed iteration scheme was incorporated into the computational model, as shown in Figure 1. An initial rotor speed was set as the initial condition. Tradeoffs had been made between computing the rapidness and accuracy by taking a nominal Reynolds number over the rotor disk at each computational frame. The Reynolds number was calculated through a blade element analysis and averaged at 0.7 R blade span stations over all of the blade azimuth stations. The ± 180 deg airfoil section lift and drag coefficients were then 2-D interpolated by the sectional effective aerodynamic angle of attack and the corresponding Reynolds number.

3. Wind Tunnel Tests of Tandem Rotor Autorotation

The wind tunnel in which these experiments were performed is a helicopter subsonic tunnel (Figure 3). Tests were taken at the open segment of the tunnel, with the maximum available wind speed being 50 m/s. The open segment has a 3.4m \times 2.4m cross section centered 3 m above ground level. To study the autorotational characteristics of the tandem rotor at different shaft angles, the tandem model fuselage was horizontally articulated to the center balance. The model was tested without blades under wind speeds of 5 m/s, 10 m/s, 15 m/s, and 20 m/s to obtain corrected data on the rotor behavior. Tests were then taken for both isolated and tandem rotor cases, for wind speeds ranging from 5 m/s to 20 m/s, collective pitch ranging from -8 deg to the value at which neither the maximum lift nor the maximum rotor speed was exceeded, and a shaft angle ranging from 5 deg to 20 deg nose up to ensure that both rotors were inside the cross-section. Test procedures were as follows:

- Isolated single-rotor tests:
 1. The fuselage was set at 180 deg of the heading angle with the rear rotor facing the incoming airflow, and only the rear rotor blade was mounted (see Figure 4). The 180 deg heading angle was adopted to reduce the aerodynamic interference from the fuselage as much as possible.
 2. The shaft angle is tuned to 10 deg and 15 deg successively.
 3. Operate the wind tunnel and set the target wind speed to 10 m/s and 15 m/s successively.

4. After the wind speed reached a steady state, we tuned the rotor collective pitch by a 1 deg increment from -8 deg to the value at which no steady rotor speed could be reached.
 5. Data including the rotor rpm and the balance forces and moments were recorded when the rotor speed reached a steady state.
- Tandem rotor tests:
 1. Set the fuselage with a 0 deg heading angle with the front rotor facing the incoming airflow with rotor blades of both the front and rear rotor mounted (see Figure 5).
 2. Steps 2 to 5 are repeated with the shaft angle from 5 deg to 15 deg (with a 5 deg increment), wind speed from 5 m/s to 20 m/s (with a 5 m/s increment), and only the data points at which a steady-state rotor speed could be reached were recorded.

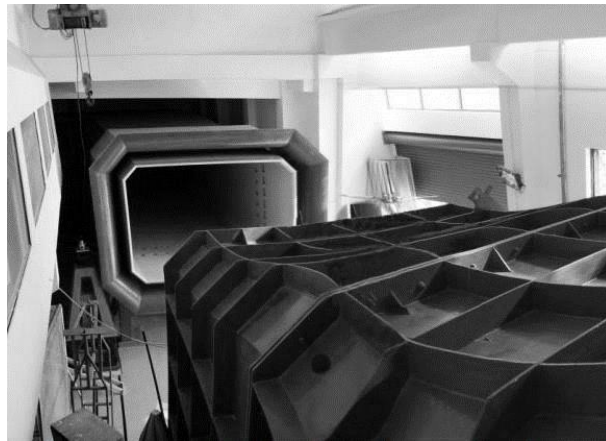


Figure 3. Helicopter subsonic wind tunnel.



Figure 4. Isolated rotor test of autorotation in forward flight.



Figure 5. Tandem rotor test of autorotation in forward flight.

The tandem model used in the experiments was composed of a front rotor, rotating clockwise when viewed from above, and a counter-rotating rear rotor, as shown in Figure 5. The front hub is higher than the rear one by 0.35 m (0.39 R) to reduce the rotor-to-rotor interference. The rotor overlap (ov), defined by $ov = 1 - d_s/d$, where d is the rotor diameter and d_s is the distance between the two rotors, is 32.5% (1.35 R). The rotor models used were two sets of three-bladed rotors. Rotor parameters are given in Table 1.

Table 1. Rotor Model Parameters.

Parameter	Value
Diameter	1.8 m
Number of blades	3
Blade length	0.8 m
Chord line	0.07 m
Rotor solidity	0.066
Blade airfoil	OA212
Blade twist	None
Flapping moment of inertia	0.064 Kg \times m ²
Rotating moment of inertia	0.192 Kg \times m ²
Lock number	5.1
Equivalent center spring stiffness	140 N \times m/rad

Several causes of the data error were known beforehand, including the shaft angle measuring error, the blade pitch error, and the wind speed deviation. The rotor hub shaft angle, i.e., the pitch attitude of the fuselage with respect to the balance center, could cause an error of ± 0.5 deg. The blade pitch error, caused by the initial tuning of collective pitch and the blade pitch servo travelling offset, would be ± 0.3 deg. The helicopter subsonic tunnel had an average sideslip airflow deflection of 0.08 deg and an axial turbulivity of 1.44% to 2.31%.

4. Analysis

4.1. Isolated Single Rotor

The rotor model from the generic helicopter flight dynamic simulation program HeliFDM is utilized in this paper to analyze the steady rotor speed of the forward autorotation state. The center spring articulated rotor of HeliFDM is blade element modelled with the dynamic blade flapping and Pitt–Peters dynamic inflow model.

Theoretical and experimental data of isolated rotor tests are shown in Figure 6, to validate the theoretical model of the isolated rotor, and to determine the tandem rotor interference. Results of wind speeds of 10 m/s and 15 m/s and shaft angles of 10 deg and 15 deg are presented, considering data sufficiency. Each test started at a collective pitch of $\theta_0 = -8$ deg, to the collective that steady autorotation can no longer be sustained. From Figure 6, we find that the maximum rotor speed occurred at approximately 1 deg collective. In the meantime, the rotor thrust shows a phased lag regarding the rotor speed, in which thrust reaches its maximum at somewhere between 3 and 4 deg of the collective pitch. $-2\text{deg} \leq \theta_0 \leq 4\text{deg}$ could be the operational range of the collective of this rotor configuration as the steady rpm varies very gently. The rotor speed dropped rather rapidly, and the rotor thrust began to decrease when θ_0 reached 4 deg, and the rpm curves are asymmetrical at the maximum rotor speed.

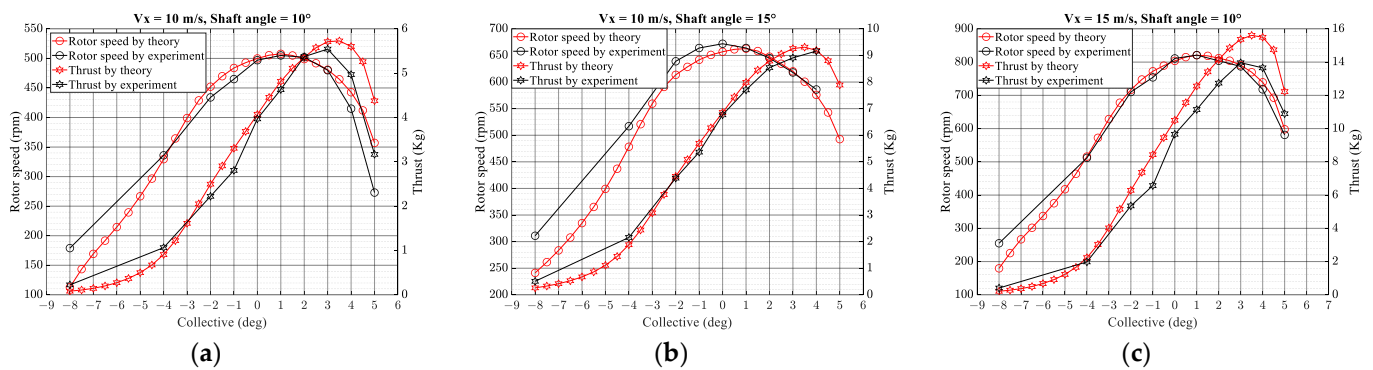


Figure 6. Comparison between experimental and theoretical rotor speed and thrust at steady autorotation: (a) $V_x = 10 \text{ m/s}$, $\theta = 10 \text{ deg}$; (b) $V_x = 10 \text{ m/s}$, $\theta = 15 \text{ deg}$; (c) $V_x = 15 \text{ m/s}$, $\theta = 10 \text{ deg}$.

The error can be seen at the maximum rpm and lower rpm at a large negative collective pitch; see the $V_x = 10 \text{ m/s}$, $\theta = 15 \text{ deg}$ case in Figure 6. As drastic changes in rotor speed occurred in the autorotating tests through the large range of the collective, the low Reynolds number effect on 2-D aerodynamic loads can have a greater impact on rotor torque than on rotor thrust thus affecting the steady autorotation rpm, since the Reynolds number affects the sectional drag coefficient much more than the lift coefficient. This can also be seen in the rather good agreement between the simulation results and test data in Figure 7, in which numerical solutions of the thrust are compared with test data by feeding the test-steady rpm to the rotor model. From Figure 7, we observe that at the same testing rpm, the rotor thrust provided by the analytical model is very close to the experimental data, with a maximum error of 5%.

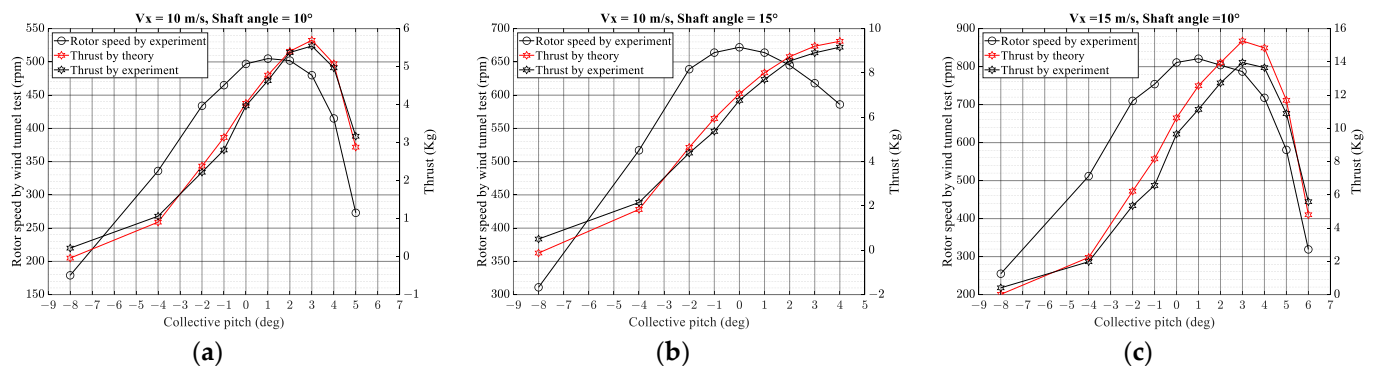


Figure 7. Comparison between experimental and theoretical thrust at steady autorotation (both thrust curves are at test-steady rpm): (a) $V_x = 10 \text{ m/s}$, $\theta = 10 \text{ deg}$; (b) $V_x = 10 \text{ m/s}$, $\theta = 15 \text{ deg}$; (c) $V_x = 15 \text{ m/s}$, $\theta = 10 \text{ deg}$.

Since the rotor rotational angular velocity is coupled with other rotor states and controls, and a transient process is also involved before the rotor speed reaches a steady state, it is generally difficult to obtain an analytical relation between the steady rotor speed and its influencing parameters via an iterative solving procedure. Figure 8 presents the disk angle of attack and driven moment of various collectives in this case. Driving/driven regions and their dominating angle of attack can be defined correspondingly. From Figure 8, we can see how the airfoil sectional drag comes into play at different steady rotor speeds. The angle of attack distribution in the outer portion of the rotor disk is believed to be the dominant region because of a higher local dynamic pressure and a longer moment arm. Thus, airfoil drag characteristics (of the outer portion of the rotor disk) in a different range of AoA affect the steady rotor rpm in a different range of collective pitch. Conclusions can be drawn as follows: In the case of the lower rpm at a large negative collective, as seen in Figure 8a,b, an airfoil drag of approximately -2 to 0 deg AoA (the outer portion of the

light blue region in Figure 8a1,b1) has a major effect of decelerating; the maximum rpm occurs at a collective near 1 deg under this flight condition and is dominated by sectional drag characteristics at a moderately positive AoA, as seen in Figure 8c, and the accelerating region (the blue portion in Figure 8c2) rotates towards the incoming flow; a lower rpm at a large positive collective is affected by drag characteristics at a moderate to stall AoA, as seen in Figure 8d1,d2. For a 5 deg collective pitch especially, rotor accelerating is dominated by near-stall AoAs, while decelerating is affected by approximately 5 deg moderate AoAs. Comparing the disk AoA and driven moment distribution, one can find that these two kinds of distribution atlases have the same pattern. To be specific, the driving moment is produced by the relatively high AoA region of the rotor disk, and vice versa.

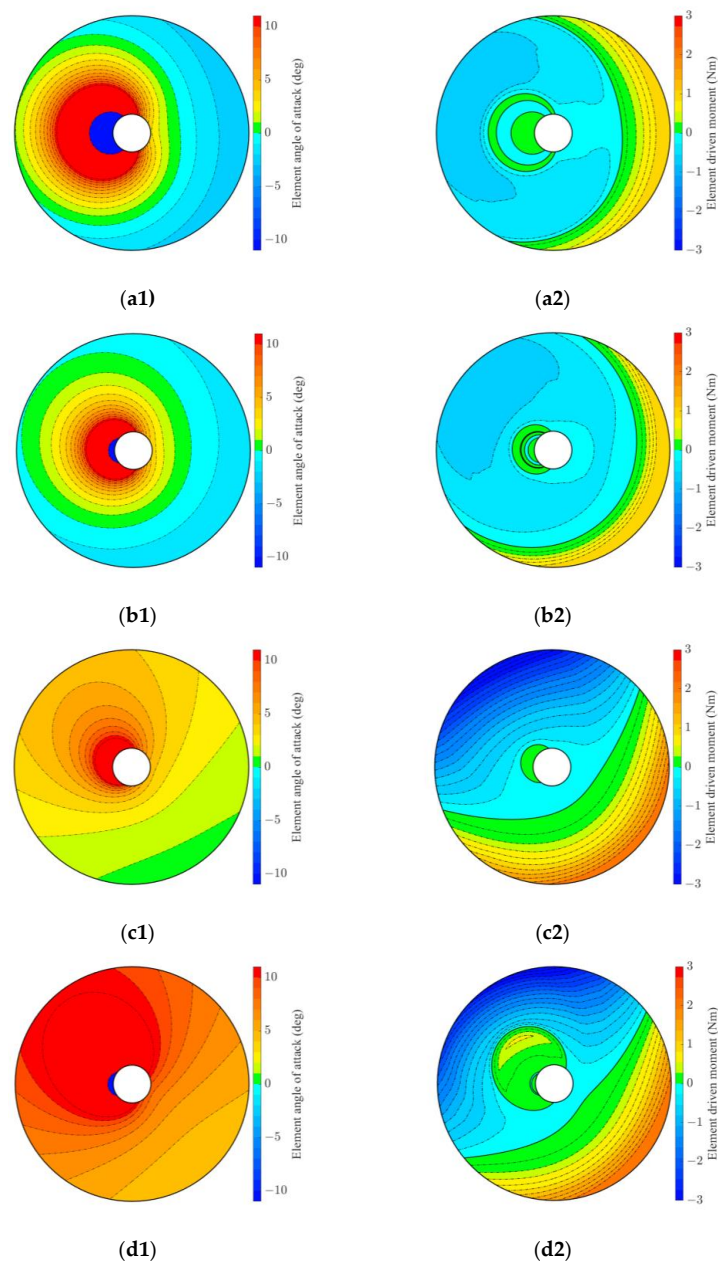


Figure 8. Blade element angle of attack and driven moment distribution of the rotor disk at $V_x = 10$ m/s, $\theta = 15$ deg: (a1) element angle of attack of $\theta_0 = -7$ deg; (a2) element driven moment of $\theta_0 = -7$ deg; (b1) element angle of attack of $\theta_0 = -4$ deg; (b2) element driven moment of $\theta_0 = -4$ deg; (c1) element angle of attack of $\theta_0 = 1$ deg; (c2) element driven moment of $\theta_0 = 1$ deg; (d1) element angle of attack of $\theta_0 = 5$ deg; (d2) element driven moment of $\theta_0 = 5$ deg.

Figure 9 summarizes the steady rpm variation with the shaft angle and wind speed as parameters. Computational results are shown at a typical wind speed of 15 m/s and a shaft angle of 15 deg. Conclusions can be drawn from Figure 9. Firstly, at a constant V_x , the operational collective range of steady autorotation shrinks with an increasing shaft angle, which is reflected in the negative-end decrease with lower shaft angles and a positive-end decrease with higher shaft angles. The decrement of the positive end of the collective is due to the stall characteristics of the airfoil. Secondly, we can find a decreasing trend in the rate of increase of the maximum steady rpm as a shaft angle increases from Figure 9a, which implies the existence of an overall maximum rotor speed in the case of a constant-rate vertical descent, i.e., a 90 deg shaft angle. Compared with Figure 9b, no such trend can be found, and the steady rpm increases with wind speed almost linearly.

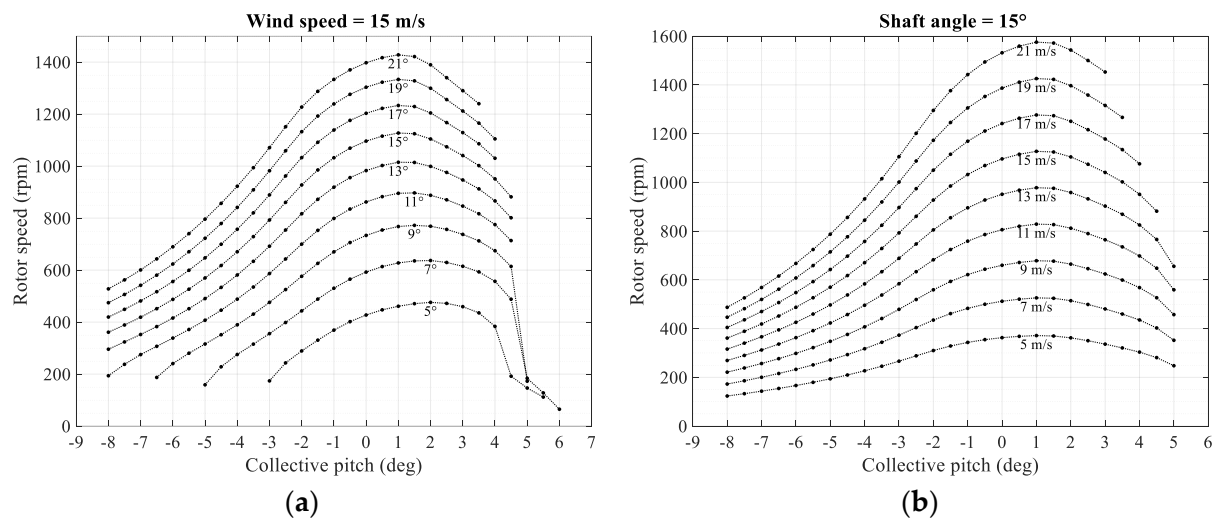


Figure 9. Rotor speed of steady autorotation at (a) $V_x = 15$ m/s, $5 \text{ deg} \leq \theta \leq 21 \text{ deg}$, (b), $\theta = 15 \text{ deg}$, $5 \text{ m/s} \leq V_x \leq 21 \text{ m/s}$.

In summary, the main conclusions that can be drawn from Figure 9a,b are that at a fixed wind speed and collective pitch, the steady rotor rpm increases with the shaft angle; at a fixed shaft angle and collective, the steady rpm increases with the wind speed; the steady rpm reaches the maximum value at a collective near positive 1 deg and then begins to drop as the collective continues to increase.

4.2. Tandem Rotor-to-Rotor Interference

4.2.1. Wind Tunnel Tests

Wind tunnel tests were performed to study the rotor-to-rotor interference of the tandem rotor in forward flight autorotation. Three flight conditions that show constructive results are presented in Figure 10. We can find a considerable rpm reduction in the rear rotor, thus causing a decrease in thrust when the collective pitch increases to a positive value under all three flight conditions. This can be accounted for by the increase in induced velocity of the front rotor, with the increase in the collective, which can cause the rear rotor to work in the strong wake of the front rotor. Compared with the isolated single-rotor rpm under the same flight condition, a slight reduction in rpm caused by the rear rotor can also be seen on the front rotor. In the meantime, the collective at which the maximum rpm of the front rotor occurs is increased due to the existence of the interference of the rear rotor.

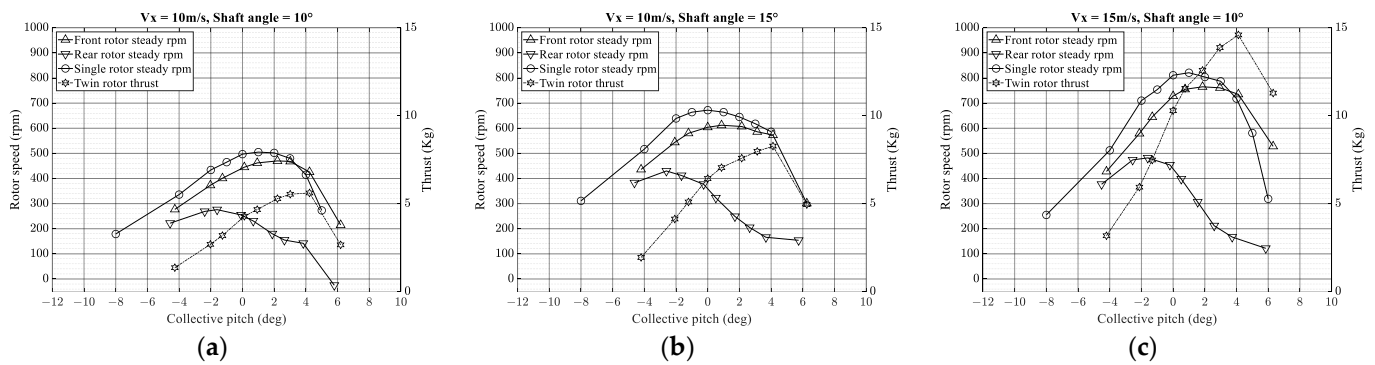


Figure 10. Wind Tunnel Data of Steady Rotor Speed of Tandem Rotor in Comparison with Isolated Rotor in Autorotation at (a) $V_x = 10\text{ m/s}$, $\theta = 10^\circ$; (b) $V_x = 10\text{ m/s}$, $\theta = 15^\circ$; (c) $V_x = 15\text{ m/s}$, $\theta = 10^\circ$.

4.2.2. Numerical Simulation

The computational fluid mechanics method is used to simulate the aerodynamic interference in forward flight autorotation by solving the governing incompressible Navier–Stokes equations of the flow field. A cubic computational domain of $40 R \times 40 R \times 40 R$ was adopted with the left and right surfaces being set to the velocity inlet with freestream velocity and pressure outlet, respectively, and the other four surfaces being set to the symmetry boundary condition as shown in Figure 11. Each rotor was enclosed by a rotating region, which performs data exchange via data interpolation with the rest of the static region. The grid layout and sliding mesh surfaces of the model are shown in Figure 12. The rotating regions are cylinders of a radius of $1.2 R$ and a height of $0.33 R$. The mesh of the whole computational domain consisted of unstructured tetrahedral grids. Mesh elements near the wall boundary of each rotor blade were refined to ensure a $y^+ = 1$ condition with boundary layer grids of 10 layers and a rate of increase of 1.2. An SST $k-\omega$ model was adopted to simulate the turbulence.

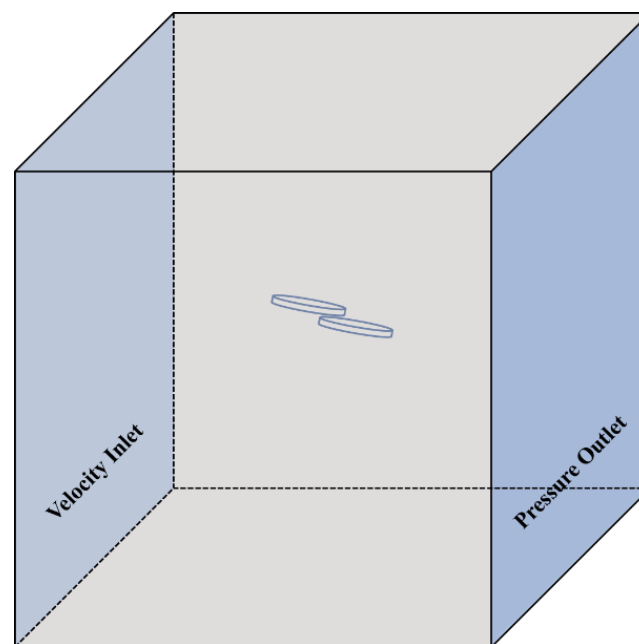


Figure 11. Computational region.

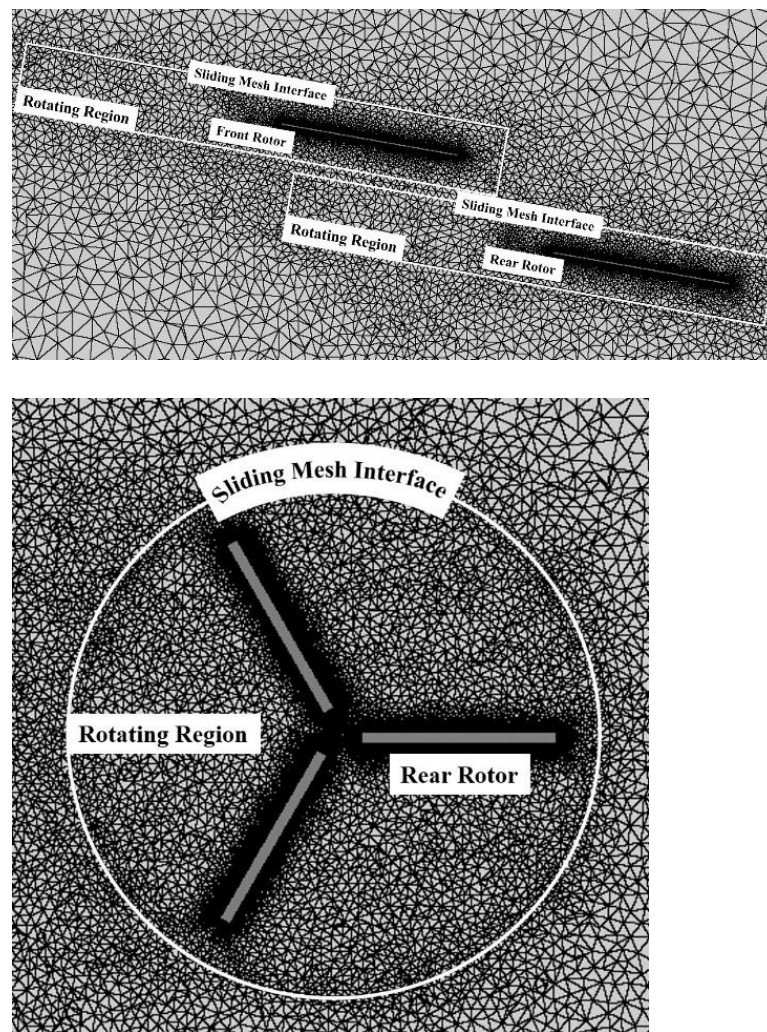


Figure 12. Grid layout and sliding mesh interface.

To verify the grid independence issue of the simulation, three sets of grids with different quantities have been adopted, which are 12.5 million, 15 million, and 28 million. Test examples were taken at a flight condition of a 15 m/s wind speed, a 10 deg shaft angle, and a 3 deg collective pitch, and the front rotor angular velocity was 761 rpm while the rear rotor angular velocity was 212 rpm. We investigated the average rotor thrust and rotor torque when the blade aerodynamic forces reach a periodic steady state. The results are summarized in Table 2:

Table 2. Rotor Thrust and Torque Under Different Grid Quantities.

Grid Quantity (Million)	Thrust (Kg)	Front Torque (Nm)	Rear Torque (Nm)
12.5	14.084	1.926	−0.021
15	13.503	1.842	−0.015
28	13.364	1.843	−0.012

As a result, considering the accuracy and available simulation time, a set of 15 million grids was adopted in this study.

Two different collectives, 3 deg and −2 deg, were chosen to perform the numerical simulation for tandem forward flight autorotation in the flight conditions tested in the wind tunnel. A collective of 3 deg is a typical state at which severe rotor-to-rotor interference occurred while a −2 deg collective could be used to compare since these states showed

relatively weak aerodynamic interference. To perform computation on autorotation states, static rotor speeds from wind tunnel tests were set as the initial values. The rotor speed is turning until the rotor torque approaches zero, which indicates the rotor is at a windmill brake state. As shown by Figures 13 and 14, periodic changes in the rotor thrust, as well as the single blade lift of both rotors, indicate the numerical convergence of the flow states. CFD results are in agreement with the wind tunnel test, as seen in Figures 13a and 14a. It is noteworthy that the difference in total thrust between the CFD and test results could be accounted for by the fact that there was a nonnegligible amount of interference caused by the rotor test bed.

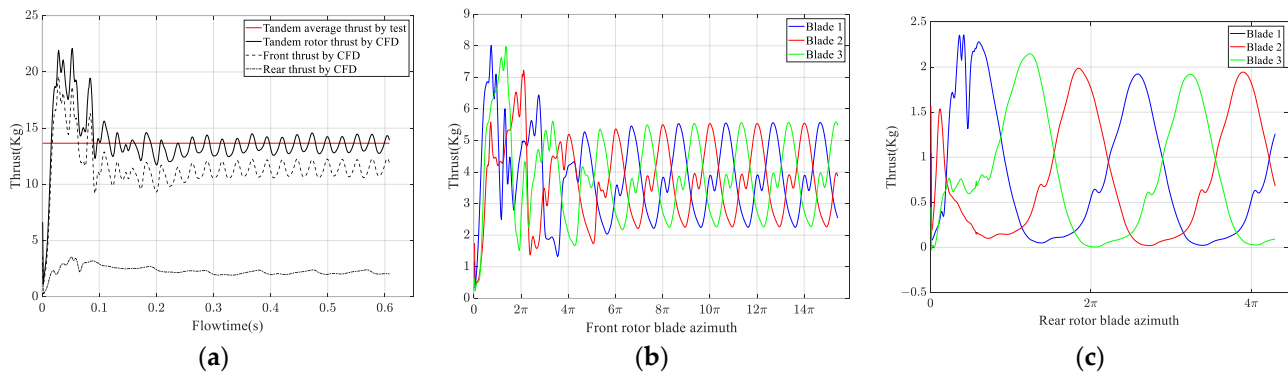


Figure 13. Numerical results of tandem rotor forward autorotation at $V_x = 15$ m/s, $\theta = 10$ deg, $\theta_0 = 3$ deg. (a) Convergence process of the rotor thrust compared with test results; (b) front rotor blade thrust; (c) rear rotor blade thrust.

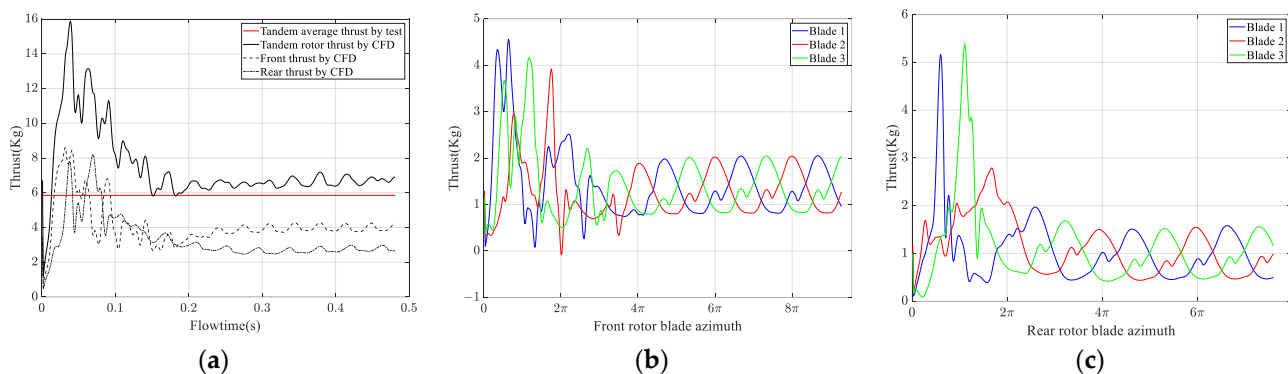


Figure 14. Numerical results of tandem rotor forward autorotation at $V_x = 15$ m/s, $\theta = 10$ deg, $\theta_0 = -2$ deg. (a) Convergence process of the rotor thrust compared with test results; (b) front rotor blade thrust; (c) rear rotor blade thrust.

From Figures 13a and 14a, we can observe the influence of the collective on the interference of the rear rotor. The upstream rotor thrust is relatively large at a 3 deg collective, which causes a larger amount of induced velocity. This is responsible for the thrust drop of the rear rotor. In contrast, at a collective of -2 deg, the rear rotor encountered a much smaller front-rotor-induced velocity. Thus, the thrust difference between the two rotors is smaller than that of the 3 deg collective situation.

Figure 15 shows the rotor-induced velocity in the rotor hub plane at a 15 m/s V_x , a 10 deg shaft angle, and a 3 deg collective. It is a typical state at which severe aerodynamic interference between rotors occurs, due to the relatively large thrust-induced velocity of the front rotor. The left-hand side of Figure 15 exhibits the hub plane of the upstream rotor while the right-hand side shows the rear rotor hub plane, which is lower than the front rotor by 0.39 R. The front rotor-induced wake at the rear rotor hub plane can be observed clearly on the right side of Figure 15.

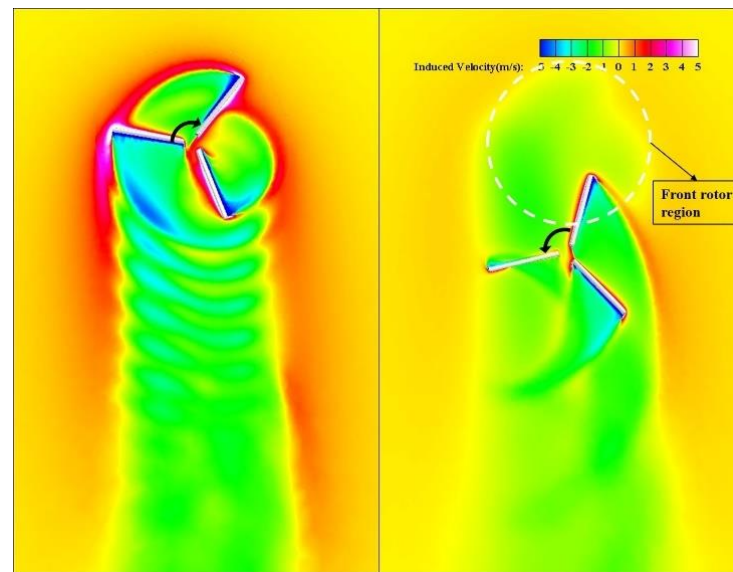


Figure 15. Rotor-induced velocity field at $V_x = 15$ m/s, $\theta = 10$ deg, $\theta_0 = 3$ deg.

The interference of the rear rotor is twofold. On one hand, the rear rotor, with a fixed rpm, suffers an evident drop in thrust due to the downwash of the front rotor, which effectively decreases the local aerodynamic AoA, just as the interference occurred on a tandem helicopter such as CH-47. This can be seen clearly on the right side of Figure 15, where the rear rotor is affected by the wake (the green region at the front part of the rear rotor) of the upstream rotor. The other aspect of interference is unique to the problems of autorotation, that is, the steady rotor rpm is further reduced by the upstream rotor wake, which is already seen via the wind tunnel test results. The cause of the reduction in the steady rpm of the rear rotor could be explained by the distribution of the induced velocity of the front rotor shown in Figure 15. One of the conclusions drawn by Figure 9a, that the steady rpm is affected by the shaft angle, needs to be discussed further here. The consequence of the shaft angle increase, from the perspective of the rotor flow field, is an increase in the AoA on the advancing side of the rotor disk and a decrease on the retreating side. Figure 15 shows an opposite scenario, which represents decreasing the shaft angle of the rear rotor. From the left of Figure 15, we can clearly find that the downwash of the front rotor on its advancing side (lower left part of the rotor disk) is larger than that of the retreating side (lower right part). This skewed downwash distribution can cause, on the rear rotor, a larger decrease in the AoA on the advancing side than on the retreating side, which in turn causes a decrease in the steady rpm of the downstream rotor.

To conclude, the interference suffered by the rear rotor in forward autorotation has two major causes: The downwash of the upstream rotor, which decreases the local AoA, leads to the decrease in the thrust of the rear rotor; the downwash asymmetry of the longitudinal axis causes a drop in the steady rpm, which further results in a decrease in rear rotor thrust.

Figure 16 shows the induced velocity distribution in the 3 deg collective situation. A relatively weak downwash can be seen on the upstream rotor. In consequence, the influence acting on the rear rotor is much smaller, as mentioned previously.

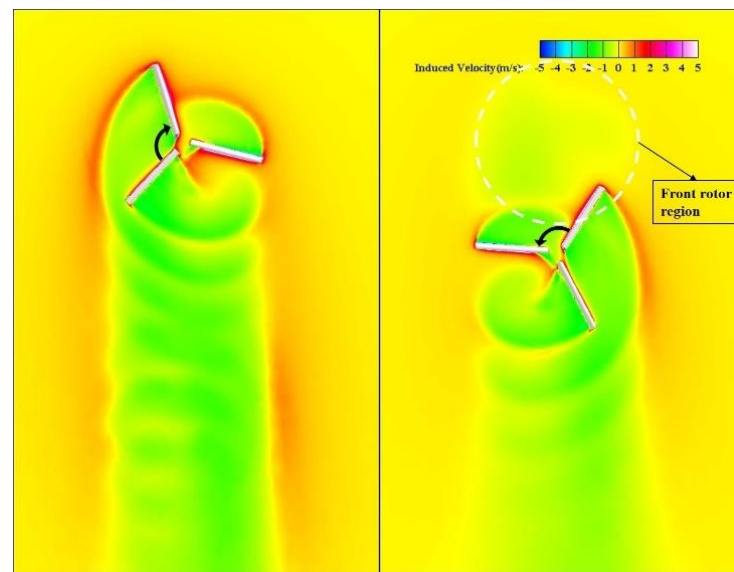


Figure 16. Roto-induced velocity field at $V_x = 15$ m/s, $\theta = 10$ deg, $\theta_0 = -2$ deg.

5. Model Refinement

The computational fluid dynamics analysis provided in the previous sections of this work revealed the details of the rotor flow field of rotor-to-rotor interference under tandem rotor forward flight autorotation states. Interference mechanisms can be explained by such a method, but this kind of analysis of the flow field also shows its apparent downside as it is extremely time-consuming and relies on the performance of computing hardware. In most engineering practices, it is preferable to balance numerical accuracy and rapidness, especially in the field of flight simulation. The isolated rotor model was modified in terms of varying the Reynolds number effect considering the drastic change in rotor speed during the transient process of autorotation to primarily predict the variation of the blade element drag affecting the rotor torque. The induced velocity was modelled by the Pitt–Peters dynamic inflow theory, in which the rotor downwash is composed of a uniform λ_0 term caused by rotor thrust and two first harmonic terms λ_{1c} and λ_{1s} due to the rotor hub aerodynamic moments. The rotor-to-rotor interference causing a steady rear rotor speed drop is primarily attributed to the fact that the rear rotor is immersed in the front rotor downwash. The front rotor wake can be considered the freestream velocity of the rear one. In consequence, the flow field of one rotor was modified by the induced velocity of the other. The major influence, i.e., the uniform induced velocity term, can be obtained by the method presented in previous sections. Empirical corrections were hence made by modifying a set of interpolation parameters using computational results.

The rotor model of the HeliFDM helicopter simulation program is refined to analyze the rotor-to-rotor interference. The mutual interference of rotors can be explained by the coupling of the induced inflow of the rotors. In the case of forward flight autorotation, the major component affecting the rotor downwash is the uniform inflow term resulting from the rotor thrust, which can be represented as follows:

$$\begin{aligned}\lambda_{0FI} &= \lambda_{0F} + \lambda_{0RF} \\ \lambda_{0RI} &= \lambda_{0R} + \lambda_{0FR}\end{aligned}\quad (10)$$

in which the uniform terms λ_{0FI} and λ_{0RI} represent the downwash of the two rotors under rotor interference. λ_{0RF} and λ_{0FR} denote the incremental terms of rear-to-front and front-to-

rear interference, respectively. Practically, the mutual interference terms can be expressed by the polynomial interpolation of the rotor inflow angle as follows:

$$\begin{aligned}\lambda_{0RF} &= (a_{1RF} + a_{2RF}\chi_R + a_{3RF}\chi_R^2 + a_{4RF}\chi_R^3)\lambda_{0R} \\ \lambda_{0FR} &= (a_{1FR} + a_{2FR}\chi_F + a_{3FR}\chi_F^2 + a_{4FR}\chi_F^3)\lambda_{0F}\end{aligned}\quad (11)$$

Parameters a_{iRF} and a_{iFR} are the polynomial coefficients of rear-to-front and front-to-rear, respectively. These coefficients are obtained by polynomial fitting, using the results of the CFD analysis. The refined model was compared to the existing experimental results and yielded relatively good agreement with the test data, as shown in Figure 17.

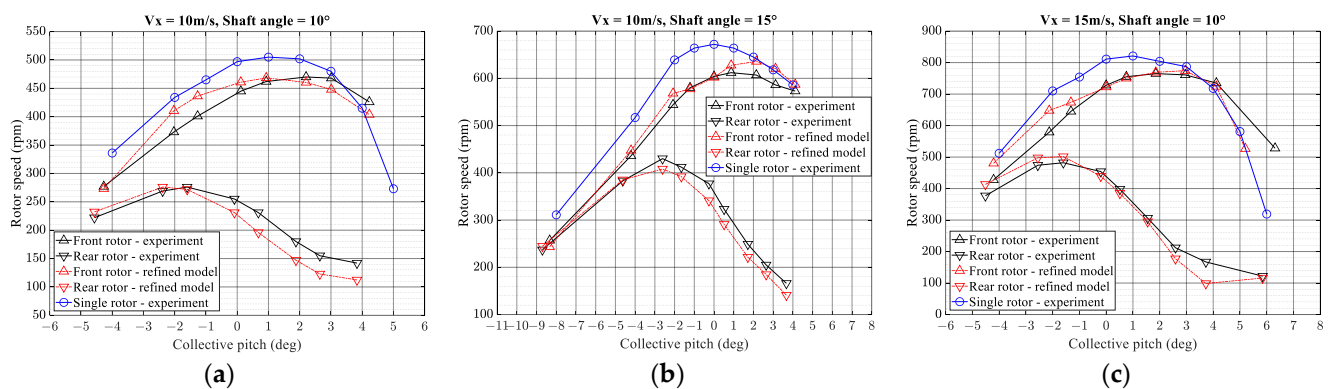


Figure 17. Refined model prediction of steady-state rotor speed of tandem rotor forward flight autorotation at (a) $V_x = 10$ m/s, $\theta = 10$ deg; (b) $V_x = 10$ m/s, $\theta = 15$ deg; (c) $V_x = 15$ m/s, $\theta = 10$ deg.

6. Conclusions

The analysis performed in this work was conducted to find the correlation of the steady-state rotor speed of a tandem configuration under rotor-to-rotor interference with three independent variables, i.e., the wind speed, the blade pitch control, and the shaft angle. This work was dedicated to establishing a systematic approach in predicting the characteristics of tandem rotor forward flight autorotation, which hence could be used both in the conceptual design of compound high-speed rotorcrafts of this configuration and in the flight dynamics analysis and simulation of tandem-rotor helicopter autorotation. The work of this paper is concluded as follows:

1. To study the tandem rotor interference cases, a single-rotor baseline model with a certain level of fidelity should be established first. A numerical model trimmed from the generic helicopter flight dynamics analysis program HeliFDM was modified by incorporating an outer $\Omega - Re$ iterative loop to compensate for the error caused by varying the Reynolds number effect on the blade section drag coefficients. The performance of the modified single-rotor model was improved by predicting the rotor torque, thus showing better accuracy when calculating the steady rotor speed and thrust. The maximum deviation of the steady rotor speed relative to wind tunnel data was 5% in the rotor collective operating range.
2. Single-rotor behavior in forward autorotation was revealed using the modified model. The pattern of distribution of the disk AoA and driven moment obtained by the single-rotor baseline model indicates that acceleration is always due to the relatively high AoA region on the rotor disk of each flight condition. The results from the disk AoA atlas play an important role in rotor blade design. The performance of autorotation could be improved by fine tuning the blade sectional drag-to-lift ratio. The variation in the steady rotor speed with the rotor collective pitch shows a nonlinear nature as it reaches its maximum at a small positive collective, which can cause the reverse of the thrust control problem when adjusting the rotor speed through the collective pitch.

In the meantime, this analysis provides an optimum operating collective pitch range (near 0 deg collective) during steady-state flight.

3. The tandem configuration was analyzed by solving the Navier–Stokes equations. Results of both rotors' induced velocity fields were obtained from the numerical simulations. These data were used to refine the rotor-to-rotor interference model by the polynomial fitting of the interfered rotor inflow. Results from the refined interference model are in good agreement with the wind tunnel data. As a result, the average percentage error of the refined model prediction of the front rotor steady-state rpm with respect to wind tunnel data is 2.1%, and that of the rear rotor is 7.5%. The resulting model of tandem rotor forward autorotation can thus be used in the overall design of compound high-speed helicopters of this kind of configuration, as well as the flight dynamic analysis of tandem rotor helicopters in a powerless descent.

In addition, some instructive results may be drawn from this work. When increasing the cruise speed, a compound tandem autogyro with thrust propellers and fixed-wing could be considered. With a lift-and-thrust compound, rotor speed, and thus rotor drag, could be considerably reduced during flight. Major difficulties in terms of flight dynamics and control of this type of aircraft could be the aerodynamic interference between rotors, as the rotor speed is not able to maintain a stable value during flight. Furthermore, the rear rotor speed could vary wildly when flight states change when collective control is applied through the flight envelope. This would cause more problems with flight stability, and even cause trouble in maintaining a trimmed flight. However, the methods utilized in this work could provide a more detailed understanding of the flight mechanics of a tandem autogyro, thus the controller could be designed via system identification using data obtained with this methodology. The rotor-to-rotor interference could also be alleviated by eliminating the overlap between two rotors, although this is not covered in this paper. A lift increase could also be practical if a convertible scheme is considered. The configuration may be implemented by a powered tandem rotor with a clutch, which could convert between a regular tandem helicopter and a tandem autogyro.

Author Contributions: Conceptualization, methodology, software, validation, formal analysis, investigation, resources, data curation, writing—original draft preparation, J.W.; writing—review and editing, Y.S.; visualization, J.W.; supervision, Y.S., H.W. and D.H.; project administration, Y.S. All authors have read and agreed to the published version of the manuscript.

Funding: This research received no external funding.

Institutional Review Board Statement: Not applicable.

Informed Consent Statement: Not applicable.

Data Availability Statement: Not applicable.

Conflicts of Interest: The authors declare no conflict of interest.

References

1. Ehinger, R.; McMenemy, M.; Wilson, P. Bell V-280 Valor: JMR TD Flight Test Update. In Proceedings of the Vertical Flight Society's 75th Annual Forum & Technology Display, Philadelphia, PA, USA, 13–16 May 2019.
2. Chery, M.C., Jr. The ABC helicopter. In Proceedings of the AIAA/AHS VTOL Research, Design, and Operations Meeting, Atlanta, GA, USA, 17–19 February 1969.
3. Bagai, A. Aerodynamic design of the X2 technology demonstrator main rotor blade. In Proceedings of the 64th Annual Forum of the American Helicopter Society, Montreal, QC, Canada, 28 April–1 May 2008.
4. Ramanujam, R.; Abhishek. Analytical and Computational Study of Hover Performance of Novel Dissimilar Coaxial Rotor. *J. Aircr.* **2022**, *59*, 1529–1544. [[CrossRef](#)]
5. Yeo, H.; Johnson, W. Aeromechanics Analysis of a Heavy Lift Slowed-Rotor Compound Helicopter. *J. Aircr.* **2007**, *44*, 17. [[CrossRef](#)]
6. Yeo, H.; Johnson, W. Optimum Design of a Compound Helicopter. *J. Aircr.* **2009**, *46*, 1210–1221. [[CrossRef](#)]
7. Yeo, H. Design and Aeromechanics Investigation of Compound Helicopters. *Aerosp. Sci. Technol.* **2019**, *88*, 158–173. [[CrossRef](#)]
8. Escobar, D.; Yeo, H. Performance and Loads of a Wing-Offset Compound Helicopter. In Proceedings of the AIAA SCITECH 2022 Forum, San Diego, CA, USA, 3–7 January 2022.

9. Houston, S.S.; Thomson, D.G. Calculation of rotorcraft inflow coefficients using blade flapping measurements. *J. Aircr.* **2009**, *46*, 1569–1576. [[CrossRef](#)]
10. Houston, S.S. Validation of a Rotorcraft Mathematical Model for Autogyro Simulation. *J. Aircr.* **2012**, *37*, 403–409. [[CrossRef](#)]
11. Houston, S.S.; Brown, R.E. Rotor-wake modeling for simulation of helicopter flight mechanics in autorotation. *J. Aircr.* **2003**, *40*, 938–945. [[CrossRef](#)]
12. Le Pape, A.; Gatard, J.; Monnier, J.C. Experimental Investigations of Rotor-Fuselage Aerodynamic Interactions. *J. Am. Helicopter Soc.* **2006**, *52*, 99–109. [[CrossRef](#)]
13. Ramasamy, M. Hover Performance Measurements Toward Understanding Aerodynamic Interference in Coaxial, Tandem, and Tilt Rotors. *J. Am. Helicopter Soc.* **2015**, *60*, 1–17. [[CrossRef](#)]
14. Brazinskas, M.; Prior, S.D.; Scanlan, J.P. An Empirical Study of Overlapping Rotor Interference for a Small Unmanned Aircraft Propulsion System. *Aerospace* **2016**, *3*, 32. [[CrossRef](#)]
15. Li, C.; Xue, C.; Bai, Y. Experimental Investigation on Aerodynamics of Non-planar Rotor Pairs in a Multi-rotor UAV. In Proceedings of the 14th IEEE Conference on Industrial Electronics and Applications, Xi'an, China, 19–21 June 2019.
16. Wang, C.; Huang, M.; Peng, X.; Zhang, G.; Tang, M.; Wang, H. Wind Tunnel Studies on Hover and Forward Flight Performances of a Coaxial Rigid Rotor. *Aerospace* **2021**, *8*, 205. [[CrossRef](#)]
17. Lee, S.; Dassonville, M. Iterative Blade Element Momentum Theory for Predicting Coaxial Rotor Performance in Hover. *J. Am. Helicopter Soc.* **2020**, *65*, 1–12. [[CrossRef](#)]
18. Guner, F.; Miller, D.G.; Prasad, J.V.R. Understanding the Effect of Rotor-to-Rotor Interference on CH-47D Helicopter Dynamics. *J. Am. Helicopter Soc.* **2021**, *66*, 1–12. [[CrossRef](#)]
19. Misiorowski, M.; Gandhi, F.; Oberai, A.A. Computational Study on Rotor Interactional Effects for a Quadcopter in Edgewise Flight. *AIAA J.* **2019**, *57*, 5309–5319. [[CrossRef](#)]
20. Healy, R.; Misiorowski, M.; Gandhi, F. A CFD-Based Examination of Rotor-Rotor Separation Effects on Interactional Aerodynamics for eVTOL Aircraft. *J. Am. Helicopter Soc.* **2022**, *67*, 1–12. [[CrossRef](#)]
21. Tan, J.F.; Zhou, T.Y.; Sun, Y.M.; Barakos, G.N. Numerical Investigation of the Aerodynamic Interaction between a Tiltrotor and a Tandem Rotor during Shipboard Operations. *Aerosp. Sci. Technol.* **2019**, *87*, 62–72. [[CrossRef](#)]
22. Padfield, G.D. *Helicopter Flight Dynamics*, 2nd ed.; Blackwell Publishing: Oxford, UK, 2007; p. 99.
23. Padfield, G.D. *A Theoretical Model of Helicopter Flight Mechanics for Application to Piloted Simulation*, RAE Technical Report 81048; Royal Aerospace Establishment: Bedford, UK, 1981.
24. Peters, D.A.; HaQuang, N. Dynamic Inflow for Practical Applications. *J. Am. Helicopter Soc.* **1988**, *33*, 64–68. [[CrossRef](#)]
25. Leishman, J.G. *Principles of Helicopter Aerodynamics*, 2nd ed.; Cambridge University Press: New York, NY, USA, 2006; p. 350.

Disclaimer/Publisher's Note: The statements, opinions and data contained in all publications are solely those of the individual author(s) and contributor(s) and not of MDPI and/or the editor(s). MDPI and/or the editor(s) disclaim responsibility for any injury to people or property resulting from any ideas, methods, instructions or products referred to in the content.